Numerical Study of Pipeline Restart of Weakly Compressible Irreversibly Thixotropic Waxy Crude Oils

Lalit Kumar, Yansong Zhao, Kristofer Paso, Brian Grimes, and Johan Sjöblom
Ugelstad Laboratory, Dept. of Chemical Engineering, Norwegian University of Science and Technology (NTNU), N-7491 Trondheim, Norway

Chris Lawrence
Institute for Energy Technology, N-2027 Kjeller, Norway

DOI 10.1002/aic.14844
Published online May 7, 2015 in Wiley Online Library (wileyonlinelibrary.com)

A 3-D axisymmetric model is developed to predict pressure wave propagation processes during gelled waxy oil pipeline restart operations. A finite volume method is implemented on a staggered grid. An iterative predictor-corrector algorithm provides solutions to the combined parabolic-hyperbolic set of governing equations. A new shear-history-dependent thixotropic rheology model is proposed for pressure wave propagation computations. Moderate Reynolds number flows within the laminar regime are computed, demonstrating the impact of inertial effects. The results clearly illustrate the important mechanisms of pipeline restart. The nature of pressure wave propagation is governed by gel strength as well as overall fluid compressibility. Three sequential pressure wave propagation regimes are dominated by inertial, viscous, and gel degradation phenomena, respectively. The viscous and gel degradation regimes are effectively coupled by imposed deformation conditions. For initially homogenous thixotropic gels, strain tends to localize near the pipeline wall, playing a central role in assuring the pipeline restart. © 2015 American Institute of Chemical Engineers
AIChE J, 61: 2657–2671, 2015
Keywords: rheology, transport, oil shale/tar sands, complex fluids, mathematical modeling

Introduction

Transport and subsea processing of waxy crude oils in extreme environments is challenging due to ubiquitous gelling and deposition phenomena. Rheological gelling processes derive from formation of percolating crystal structures in which a volume-spanning network of solid crystals occludes the remaining liquid. The structural formation process modulates rheological properties of the crude oil.[1–4] At petroleum production fields and installations, occasional flow outages are unavoidable, due to maintenance and remediation requirements. Environmental thermal losses result in significant temperature reduction of the pipeline fluid. When the fluid temperature falls below the wax appearance temperature, paraffin waxes precipitate.[3] Further temperature reduction drives the formation of a significant solid fraction, resulting in gel formation and non-Newtonian behavior. In this study, the combined effect of inertia, viscosity, and gel breakdown on pressure propagation is investigated with the intent to facilitate development of useful analytical simulation tools for pipeline restart applications.

Flow restart in gelled pipe segments requires application of a substantial axial pressure drop. The overall flow commencement process entails several transient subprocesses. The current report is intended to provide a new exploratory and developmental analysis of the role of several of the transient subprocesses in the overall flow commencement process. The overall aim of the report is to advance simulation technologies available for the purposes of field architecture design, production risk assessment, flow assurance, inhibitor dosage optimization, and emergency intervention planning.

The current investigation is differentiated from previous pipe simulation investigations[5–13] by presenting for the first time appropriate scale-up of strain-dependent viscous rheologies to pipeline time and length scales. Previous published pressure wave propagation models rely on explicit time dependent rheologies.[5–13] Strain-dependent predictions of the attenuated acoustic wave, the viscous diffusion wave, and the gel degradation wave are presented in the current report for the first time. Inclusion of strain-dependent creep and gel degradation responses within the rheology comprises (from a theoretical perspective) a large step forward in affording accurate, realistic, and determinative pipeline restart simulations.

Theory

When a high pressure condition is applied at the pipe inlet, pressure is transmitted axially along the pipeline length by propagation of acoustic, viscous, and gel degradation

Current address of Yansong Zhao: Energy and Climate Group, Dept. of Physics and Technology, UiT The Arctic University of Norway, N-9037 Tromsø, Norway
Current address of Chris Lawrence: SPT Group, N-2027 Kjeller, Norway
Correspondence concerning this article should be addressed to L. Kumar at this current address: Dept. of Mechanical Engineering, University of British Columbia, 2054-6250 Applied Science Lane, Vancouver, BC V6T 1Z4, Canada; e-mail: lalitk@gmail.com and lalitk@mail.ubc.ca.

pressure waves. Subsequently, creeping flow may occur with concomitant gel degradation. Finally, if sustainable outlet flow commences, transient flow acceleration may accompany the pipeline clearing process. Successful pipeline restart operations result in large scale steady state flow. Thermal shrinkage coupled with gas release results in gas pocket formation during cooling. Concomitant density variations may arise. Hence, a radially averaged and local axially-averaged compressibility approach is employed.

For more than four decades, many researchers have studied pressure propagation and restart processes for pipelines filled with waxy crude oil. Cawkwell and Charles[5,6] simulated a 1-D compressible thixotropic pipeline flow. Results were compared with earlier work on incompressible flow.[10] Compressibility was incorporated within an isothermal context. Cawkwell and Charles found that compressible gels required ~42% lower clearing time compared to incompressible gels to dislodge waxy crude from the pipeline. Recently, more studies related to pipeline restart were performed for weakly compressible gels. A 3-D axisymmetric geometry was simulated for a Bingham fluid by Vinay et al.[11] Furthermore, a computation scheme was also developed by Wachs et al.[13] in which the axial velocity is allowed to vary with both axial and radial position with the assumption of zero radial velocity. They refer to this model as a 1.5 dimensional simulation. In these works, a rigorous Lagrangian multiplier mathematical analysis was performed to treat nondifferentiability associated with a Bingham/Houska rheology.[14] However, real waxy crude gels exhibit demonstrable creep under stress. The Bingham/Houska construct is a theoretical concept for describing complex phenomena using simple constitutive relations. The scheme has two distinct disadvantages for use in pipeline restart simulators. First, the construct exhibits a discontinuity which causes numerical instabilities within the calculation algorithm. Second and more importantly, the rheology is not representative of creep phenomena. Thus, this work does not adopt the Bingham/Houska rheology.

In this work, a creep approach is adopted within the framework of an apparent viscosity coefficient. Creeping flow has been observed at applied stress conditions lower than the effective yield stress.[15–18] Creep is modeled, in a first approximation, by a corresponding high viscosity condition.[19,20] Creep results in deformation, which imparts structural degradation to the gel. Degradation processes are modeled by a reduction in viscosity, which facilitates restart. In this investigation, the creep viscosity is established as a strain-dependent apparent viscosity which is assigned a very high value ($\sim 10^2$ Pa.s–10^4 Pa.s) initially, at low strains. The gel state is assumed to follow a point function of absolute strain instead of time.[21–23] Hence, a strain-dependent apparent viscosity is established without a true yield stress. Gelled waxy crude oil may be classified as an irreversible thixotropic material with a known degradation and breakdown behavior. Subsequent to breakdown, crystal-crystal bonds are not immediately reformed. Gel degradation kinetics has previously been established as a first-order (exponential decaying[7,24,25]) and third-order process with respect to absolute imposed strain or time.[21,23] Here, first-order and third-order degradation kinetics means that the rate of gel structure breakage is a first-order or third-order function of the structural parameter, respectively.

Multiplug gel conditions have previously been addressed by Davidson et al.[9] using a Bingham rheology formulation where yield stress and viscosity are point functions of time. Incompressible and compressible 1-D flow have also been modeled by Chang et al.[7] and Davidson et al.[8] using a semianalytical approach. Recently, rigorous experiments have been performed by Borghi et al.,[26] Margarone et al.,[27] Magda et al.[28] and El-Gendy et al.[29] to analyze pressure wave propagation processes. Adhesive vs. cohesive failure has been discussed by Lee et al.,[2] Jemmett et al.,[30] and Kumar et al.[31] with strong implications for internal vs. near-wall breakdown processes.

In the current investigation, a homogeneous initial state is assumed. For the homogenous initial gel conditions, the gel strength profile becomes nonhomogeneous in the axial and radial directions as a result of deformation and degradation. For homogenous gels, near-wall breakdown processes are responsible for reducing pressure drop requirements for flow commencement. In the case of homogenous initial gel conditions, both the degree of deformation and the stress level reach a maximum near the wall. Therefore, both cohesive and adhesive breakage will be initiated near the wall for homogenous gel conditions. Internal failure or core failure on the other hand, is associated with strong radial heterogeneity.

In this study, strain evolution is incorporated for the first time within a rheology formalism based on apparent viscosity. A homogeneous waxy crude oil gel is assumed to be initially at rest. At time $t = 0^+$, a large constant pressure is applied at the pipeline inlet using displacing fluid. The displacing fluid has a constant steady state value of viscosity. A finite volume method on a staggered grid is verified by computation of known Newtonian compressible flows. Further verification of the model is established by confirmation of an equivalence between the initial pressure wave propagation speed and the acoustic speed for weak gel conditions. Moreover, a systematic analysis for convergence and grid dependency is presented in result and discussion section.

Strain evolution is ascertained by real-time tracking of the deformation state using a newly developed algorithm. Three primary phenomena facilitate initial pressure transmission and flow restart in the pipeline: (1) Inertial compression, (2) strain accumulation, and (3) gel breakdown. When high pressure is applied across the pipeline, a fluid element undergoes inertial compression when the acoustic wave passes through the local pipeline segment. In the absence of instantaneous adhesive failure, the gel remains in a no-slip condition at the wall, which results in the development of strain near the wall. Concomitant strain accumulation by viscous shearing leads to gel breakdown. These phenomena result in a highly nonuniform strain distribution across the pipeline in both the radial and axial directions, causing heterogeneity in gel structure. In the final stage, accumulated strain leads to significant reduction in viscosity and facilitates pipeline restart. This reasoning leads to the hypothesis that strain is relatively localized near the pipe wall. As such, radial shear localization and axial stress localization comprise two essential subprocesses which facilitate timely restart processes.

Conservation equations

The physical processes of restart are described by the following system of equations

Conservation of mass

$$\frac{\partial \rho}{\partial t} + \nabla \cdot (\rho \mathbf{U}) = 0 \tag{1}$$

In this relation ρ represents fluid density, $\boldsymbol{U}$ denotes velocity field, t represents time and $\frac{D}{Dt} = \frac{\partial}{\partial t} + \boldsymbol{U} \cdot \nabla$ is convective

time derivative. For isothermal flow, this can be expressed in terms of the pressure p

$$\chi_\Theta\left(\frac{\partial p}{\partial t}+\mathbf{U}\cdot\nabla p\right)+\nabla\cdot\mathbf{U}=0 \tag{2}$$

In this relation, $\chi_\Theta=\frac{1}{\rho}\left(\frac{\partial\rho}{\partial p}\right)_\Theta$ denotes the isothermal compressibility.

Neglecting hydrostatic effects, the momentum balance is expressed as

$$\rho\left(\frac{\partial\mathbf{U}}{\partial t}+\mathbf{U}\cdot\nabla\mathbf{U}\right)=\nabla\cdot\boldsymbol{\sigma} \tag{3}$$

The stress tensor σ is

$$\boldsymbol{\sigma}=-p\mathbf{I}+\boldsymbol{\tau} \tag{4}$$

In this relation, $\boldsymbol{\tau}$ represents a deviatoric stress tensor which follows a pseudo Newtonian behavior

$$\boldsymbol{\tau}=2\mu\boldsymbol{d}+\left(\left(\xi-\frac{2}{3}\mu\right)\nabla.\boldsymbol{U}\right)\boldsymbol{I} \tag{5}$$

where μ is viscosity and ξ is the secondary viscosity which is assumed to be zero. Furthermore, divergence of velocity is neglected within the momentum relation for a weakly compressible fluid. Waxy crude oil gels creep under applied stress. Therefore, creep viscosity is assumed to follow the form given by Eq. 6, where viscosity is defined as a point function of absolute strain

$$\mu=\mu_0(1+k(1-\exp(-m_0\gamma))/\gamma) \tag{6}$$

In the above rheological relation, m_0 represents a kinetic structural degradation rate parameter. The parameters $k=\frac{\mu_g}{m_0\mu_0}$ and μ_g is the initial gel viscosity represents gel strength. Our rheological model is consistent with Ronningsen first-order gel degradation kinetic rheological model[25] at low value of strain. Taking into consideration the Taylor expansion of Eq. 6 along with the fact that at initial stage of gel deformation strain is linearly correlated with time, our rheological model reduces to first-order gel degradation kinetic rheological model presented by Ronningsen.[25] For high value of strain, our rheological model is consistent with second-order gel degradation kinetics viscosity reduction given by Ronningsen.[25] Moreover, Wardhaugh and Boger,[32] categorize the rheology of crude oil into three different regimes, the first regime is a Hookean like elastic behaviour followed by creeping flow, which leads to fracture of the gel. In our model, elastic behaviour of crude oil is approximated by constant but very high viscosity. This is possible as under applied stress fluid deforms slowly. Slow deformation can be associated to very small strain rate. Hence, high viscosity of the gel along with small shear rate also explains high stress during slow deformation. The variation of viscosity for our rheological model as a function of the absolute strain is presented in Figure 1 along with the third-order structural decay relation

$$\mu=\mu_0\left(1+k^1/(1+2m_0\gamma)^{0.5}\right) \tag{7}$$

In Figure 1, μ_0 is 0.5 pa.s, $m_0$is 100, k^1 is 20,000, and k is 200. The equation governing strain evolution is approximated as

$$\frac{D\gamma}{Dt}=\|\boldsymbol{d}\| \tag{8}$$

In this relation, $\boldsymbol{d}=\frac{1}{2}(\nabla\mathbf{U}+(\nabla\mathbf{U})^T)$ is the rate of strain tensor, γ is the representative strain, and D/Dt is the convective time derivative and $\|.\|$ Corresponds to the Euclidian norm, defined as

$$\|\boldsymbol{d}\|=\left(\frac{1}{2}\sum_{1\le i,j\le d}|d_{ij}|^2\right)^{1/2}$$

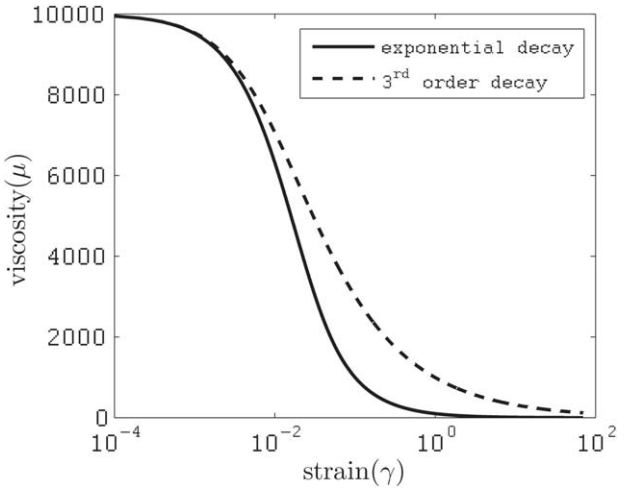

Figure 1. Viscosity variation with absolute strain for exponential decay as well as third-order decay.

Flow Geometry and Boundary Conditions

A 3-D-axisymmetric pipe geometry in cylindrical coordinates is shown in Figure 2. The azimuthal component of velocity is zero (symmetry). Boundary conditions are expressed as follows.

- At the inlet, Dirichlet conditions are prescribed for pressure, strain, radial velocity component, and axial stress component

$$u=\tau_{zz}=0$$

$$p=p_{\text{inlet}},\gamma=\gamma_{\text{inlet}}$$

The value of γ_{inlet} determines the nature of the displacing fluid. If the displacing fluid is assumed to be fresh crude oil, with steady state rheological properties, then $\gamma_{\text{inlet}}=5000$ is assigned which gives viscosity value$\mu_0\sim$0.5 pa.s. On the other hand, if the displacing fluid is similar to the shut-in gel, γ_{inlet} has a zero value.

- At the outlet, Dirichlet conditions are imposed on the radial velocity component, axial component of the extra-stress tensor, and pressure, with a Neumann condition on the strain

$$u=\tau_{zz}=\partial\gamma/\partial z=0$$

$$p=p_{\text{outlet}}=0$$

- At the wall, a no-slip condition is set on the velocity

$$u=w=0$$

- Along the center of the pipe, a symmetry boundary condition is applied

$$u=0,\tau_{rz}=\partial\gamma/\partial r=0$$

In addition to boundary conditions, quiescent initial conditions are assumed: no flow, pristine gel condition inside the

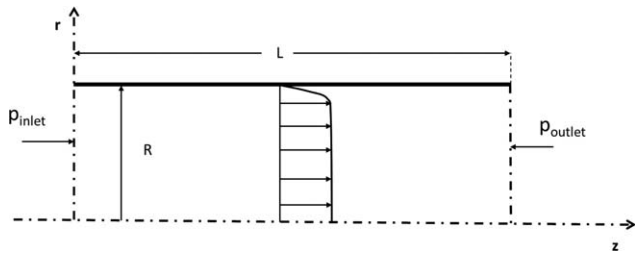

Figure 2. Schematic diagram showing the computational domain.

pipeline ($\gamma = 0$) and the pressure inside the pipeline is equal to the exit pressure.

Mathematical Formulation

The following viscous scaling scheme is used

$$\begin{cases} L_s = \dfrac{PR}{2\tau_s} & W_s = \dfrac{R\tau_s}{2\mu_0} & \varepsilon = \dfrac{R}{L_s} & \mu_r = \dfrac{\mu(\gamma=0)}{\mu_0} \\ \hat{\mu} = \dfrac{\mu}{\mu'_0} & \hat{\mu}_0 = \dfrac{\tau_s}{P} & Re^* = \dfrac{\rho_0 R W_s}{2\delta\mu'_0} & \hat{t} = \dfrac{t}{L_s\delta/W_s} \\ \hat{z} = \dfrac{z}{L} & \hat{r} = \dfrac{r}{R} & \hat{w} = \dfrac{w}{W_s} & \hat{u} = \dfrac{u}{\varepsilon W_s} \\ \hat{d} = \dfrac{d}{W_s/L_s} \end{cases} \tag{9}$$

R denotes the pipeline radius, $P = (p_{in}-p_{out})$ is the applied pressure difference across the pipeline where p_{in} is the applied inlet pressure and p_{out} is the outlet pressure, μ ($\gamma = 0$) is the dimensional viscosity of pristine gel, μ_0 is the steady state crude oil viscosity, and W_s is the axial velocity scale. The variable group εW_s is the radial velocity scale. The radial velocity scaling is selected on the basis of a low radial flow condition, such that the dimensionless radial velocity is of order unity. The parameter τ_s is a typical value of the stress required for the scaling, which has no effect on the results. L is the pipeline length, and also serves as the axial length scale. L_s is the limiting pipeline length for restart of the pipeline in the case of incompressible Bingham gels. The variable group $L_s\delta/W_s$ is a timescale which accounts for fluid movement as well as pressure propagation. Hence, the timescale incorporates the applied pressure, compressibility and steady state crude oil viscosity. Re^* denotes the scaled Reynolds number and ρ_0 denotes the crude oil density at the outlet pressure. The strain rate is scaled by W_s/L_s, and μ'_0 is a rescaled viscosity defined as $\mu'_0 = \mu_0 \frac{P}{\tau_s}$.

In addition to the characteristic scales defined above, other key quantities are:

- The steady state Reynolds number

$$Re_{ss} = \frac{\rho_0 R w_{max}}{\mu_0}$$

- The pressure scaled by the applied pressure difference

$$\hat{p} = \frac{p - p_{out}}{p_{in} - p_{out}} = \frac{p}{P}$$

- The compressibility number

$$\delta = \chi_\Theta P$$

and α is the ratio of actual pipeline length and L_s.

The scaled conservation equations are expressed as follows

$$\frac{\partial\hat{p}}{\partial\hat{t}} + \delta\left(\hat{u}\frac{\partial\hat{p}}{\partial\hat{r}} + \frac{\hat{w}}{\alpha}\frac{\partial\hat{p}}{\partial\hat{z}}\right) + \hat{\Delta} = 0 \tag{10}$$

$$\hat{\Delta} = \hat{u}\hat{r} + \frac{\partial\hat{u}}{\partial\hat{r}} + \frac{1}{\alpha}\frac{\partial\hat{w}}{\partial\hat{z}}$$

$$\varepsilon^2 Re^* \exp(\delta\hat{p})\left\{\frac{\partial\hat{u}}{\partial\hat{t}} + \delta\left(\hat{u}\frac{\partial\hat{u}}{\partial\hat{r}} + \frac{\hat{w}}{\alpha}\frac{\partial\hat{u}}{\partial\hat{z}}\right)\right\} + \frac{\partial\hat{p}}{\partial\hat{r}} = \frac{1}{2}\varepsilon\left(-\frac{\hat{\mu}\hat{u}}{\hat{r}^2} + \frac{1}{\hat{r}}\frac{\partial\hat{r}\hat{\mu}(\partial\hat{u}/\partial\hat{r})}{\partial\hat{r}} + \frac{\varepsilon^2}{\alpha^2}\frac{\partial\hat{\mu}(\partial\hat{u}/\partial\hat{z})}{\partial\hat{z}}\right) \tag{11}$$

$$Re^* \exp(\delta\hat{p})\left\{\frac{\partial\hat{w}}{\partial\hat{t}} + \delta\left(\hat{u}\frac{\partial\hat{w}}{\partial\hat{r}} + \frac{\hat{w}}{\alpha}\frac{\partial\hat{w}}{\partial\hat{z}}\right)\right\} + \frac{1}{\alpha}\frac{\partial\hat{p}}{\partial\hat{z}} = \frac{1}{2\varepsilon}\left(\frac{1}{\hat{r}}\frac{\partial r\hat{\mu}(\partial\hat{w}/\partial\hat{r})}{\partial\hat{r}} + \frac{\varepsilon^2}{\alpha^2}\frac{\partial\hat{\mu}(\partial\hat{w}/\partial\hat{z})}{\partial\hat{z}}\right) \tag{12}$$

$$\|\hat{d}\| = \sqrt{\hat{d}_{zr}^2 + \frac{1}{2}\left(\hat{d}_{rr}^2 + \hat{d}_{\theta\theta}^2 + \hat{d}_{zz}^2\right)} \tag{13}$$

$$\frac{\partial\hat{\gamma}}{\partial\hat{t}} + \delta\left(\hat{u}\frac{\partial\hat{\gamma}}{\partial\hat{r}} + \frac{\hat{w}}{\alpha}\frac{\partial\hat{\gamma}}{\partial\hat{z}}\right) - \hat{d}\delta = 0 \tag{14}$$

Numerical Solution

In the finite volume formulation, the calculation domain Ω is subdivided into a finite number of control volumes. The control volumes for specific variables (i.e., u,w,γ and p) are located at staggered positions (for details see Kumar et al.[31]). The control volume for strain coincides with the control volume for pressure. The details of numerical methods can be found in Kumar et al.[31] Kumar et al.[31] have disccused some of the results for pressure propagation in homogenous and hetrogenous gel without looking details of restart process. Moreover, the time scaling in their simulation makes calculation of restart process computational very expensive.

Results and Discussion

The presented 3-D axisymmetric model provides predictions for pipeline restart based on strain-dependent flow rheology. The code is checked against two limiting cases: (1) weakly compressible Newtonian flow, and (2) acoustic pressure transmission. Moreover, a systematic analysis of the error associated with discretization is presented in Table 2. When pressure propagates at the acoustic velocity, the pressure gradient attains a maximum value at the compression front, and this sharp pressure gradient is difficult to capture. Successful verification of the acoustic wave propagation process confirms the robustness of the numerical model. The computations emulate real time flow evolution for initial homogenous gel conditions. Effects of gel strength, compressibility, Reynolds number, and thixotropy are investigated. Finally, it is shown that the strain localizes near the wall for homogeneous gels.

The initial conditions reflect a pristine and quiescent gel state at time $\hat{t} = 0$. The initial pressure within the pipeline is assumed to be identical to the outlet pressure. At time $\hat{t} = 0^+$, a constant pressure is applied at the pipe inlet by a

Table 1. The Value of Non-Dimensional Parameters Used in This Study

Parameters	Values
L/R	80–1760
δ	4×10^{-2}–4×10^{-6}
Re_{ss}	56–1056
μ_r	2×10^{2}–2×10^{4}
α	0.8–17.6
ε	0.01–0.16

displacing fluid whose properties are defined by γ_{inlet}. The displacing fluid is outside the simulation box, and only comes into existence once it enters $\hat{z} \geq 0$. The results are presented using non-dimensional coordinates ($\hat{r} = r/R$ and $\hat{z} = z/L$ and nondimensional time ($\hat{t} = t/(L_s\delta/W_s)$). Therefore, dimensionless time values are not directly comparable for dissimilar cases. However, when necessary, time scales are converted to an identical scaling to facilitate appropriate comparison. In addition, a dimensional form is presented to facilitate appropriate interpretation. The dimensional pressure varies from 10^2 to 10^6 Pa and the actual compressibility varies from 10^{-10} to 10^{-6} Pa^{-1}. The flow geometry dimensions correspond to L/R ratios of 50 to 2000. Dimensionless steady state viscosity and aspect ratios are selected as $\hat{\mu}_0 = 8.18/(2Re_{ss})$ and $\varepsilon = 8.18/Re_{ss}$, respectively. Therefore, we choose $\tau_s = 200$ Pa to give a desired aspect ratio (L_s/R) = 100 at $Re_{ss} = 818$. The dimensional pipe length is given by $L = \alpha L_s$. The parameter α is equivalent to the Bingham number defined within the Bingham rheology approach. The summary of parameters used in this study are given in Table 1.

Effect of mesh size

A structured Cartesian mesh with uniform grid size in each direction is generated for the computational geometry. The numbers of grid cells in the radial and axial directions are denoted by N_r and N_z, respectively. Variation of the mesh size is considered to investigate grid dependence and solution convergence. A summary of their characteristics is presented in Table 2.

The effects of the mesh size in the radial direction are investigated by comparing the value of the fully developed steady state axial velocity for Newtonian flow with the analytical solution. The fully developed steady state velocity profile for Newtonian flow can be easily derived analytically. The error "Error$_r$" between numerical simulated and analytical axial velocity is defined as the maximum value along the pipe centerline of the quantity

$$\text{Error}_r = \frac{|\hat{w}_{computed} - \hat{w}_{analytical}|}{\hat{w}_{analytical}} \tag{15}$$

The error "Error$_r$" is calculated for each mesh size presented in Table 2 for all grid points and the maximum value of "Error$_r$" is reported. The accuracy of axial velocity should depend on radial grid size. This is confirmed in Table 2, where, except in the case of very few axial grid cells, for example, mesh number 3, the axial velocity convergence does not depend on the number of axial grid cells. In Table 2 for meshes 4 to 9, the increase in the number of grid cells in the axial direction does not improve the accuracy of the axial velocity. Hence, the correct prediction of the axial velocity depends only on the radial grid resolution. Furthermore, from Table 2 it is clear that with the increase in the number of grid cells in the radial direction, the axial velocity converges toward the analytical solution. However, due to finite computational resources the radial grid number N_r =20 has been chosen for further calculations. This particular choice gives error less than 0.1%.

The effect of N_z is assessed on the fully developed pressure profile for Newtonian flow. After the previous analyses, N_r is fixed at 20 and N_z is varied from 30 to 300 (mesh 3 to 9). The relative error between analytical and numerical solutions for the fully developed pressure profile is calculated. The fully developed steady state pressure profile for Newtonian flow can be easily derived analytically. The error "Error$_z$" between numerical simulated and analytical pressure is defined as the maximum value along the pipe centerline of the quantity

$$\text{Error}_z = \frac{|\hat{p}_{analytical} - \hat{p}_{computed}|}{\hat{p}_{analytical}} \tag{16}$$

From Table 2, it is clear that for all the grid sizes, the steady state pressure profile gives a small error of order 0.02%. However, the steady state pressure profile is linear and easy to predict. Therefore, it is important to find a more robust test of the axial grid dependence and convergence. For this purpose, the convergence of the pressure profile for thixotropic flow for a particular time has been analyzed. There is no analytical solution for thixotropic weakly compressible fluid. Hence, a different criterion has been used to define the error. The relative error between two meshes has been computed for weakly compressible irreversible thixotropic fluid pressure profile as

$$\text{Error}_{z1} = \frac{|\hat{p}_{avg}(N_z) - \hat{p}_{avg}(300)|}{\hat{p}_{avg}(300)} \tag{17}$$

where $\hat{p}_{avg} = \int_0^1 \hat{p}\, d\hat{z}$ is the average pressure in the pipeline and N_z is the number of cells in the axial direction. The average pressure value for the finest grid is used as a reference value to analyze the convergence of the solution. The result is presented in Figure 3a. Figure 3a shows that the solution converges systematically and the trend confirms the grid independent solution. The effect of using $N_z = 300$ as the reference value is indicated by the vertical asymptote in Figure 3a. Clearly, the error approaches zero as N_z approaches 300 as would be expected. Nevertheless, the true convergence is also indicated by the line with slope -1. From Figure 3a and Table 2, it is also clear that relative error is of order 0.2%–0.5% for grid number 200. Hence, in

Table 2. The Effect of Mesh Size on the Accuracy of the Solution

Meshes	$N_r \times N_z$	Error$_r$	Error$_z$ for Newtonian Flow	Error$_{z1}$ for Thixotropic Flow
Mesh1	10 × 50	3.7×10^{-3}		
Mesh2	15 × 200	1.6×10^{-3}		
Mesh3	20 × 30	3.1×10^{-2}	1.93×10^{-4}	0.0287
Mesh4	20 × 50	9.2×10^{-4}	1.96×10^{-4}	0.0161
Mesh5	20 × 100	9.3×10^{-4}	1.98×10^{-4}	0.0066
Mesh6	20 × 150	9.3×10^{-4}	1.98×10^{-4}	0.0032
Mesh7	20 × 200	9.3×10^{-4}	2.00×10^{-4}	0.0016
Mesh8	20 × 250	9.0×10^{-4}	2.01×10^{-4}	0.0006
Mesh9	20 × 300	8.1×10^{-4}	2.02×10^{-4}	
Mesh10	25 × 200	5.9×10^{-4}		

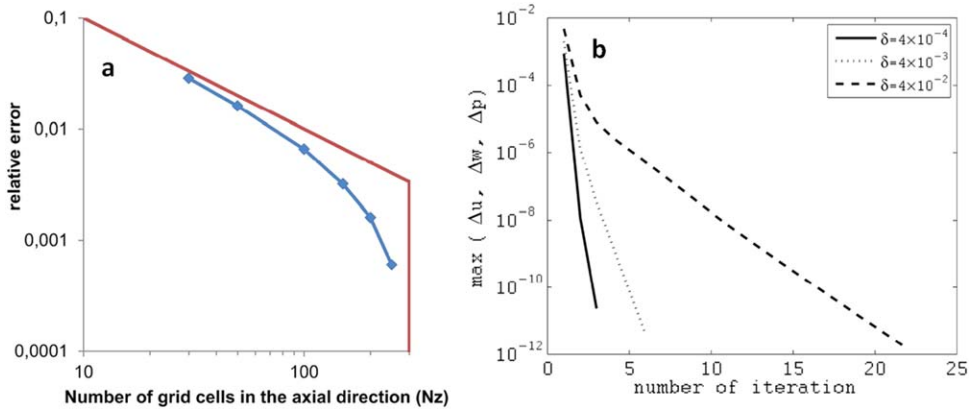

Figure 3. (a) The effect of axial grid size on the relative error and (b) the effect of compressibility number on the convergence of the numerical algorithm for with parameters $\delta = 4\times10^{-4}$, $\alpha = 1.1$, and $Re_{ss} = 818$.

[Color figure can be viewed in the online issue, which is available at wileyonlinelibrary.com.]

this article, $N_r = 20$ and $N_z = 200$ are used for simulation, which is a good compromise between accuracy and simulation time requirement.

Solution convergence

An iterative approach is used at all time-steps. This approach is similar to steady state calculations, assuring convergence. Figure 3b shows convergence characteristics at various compressibility numbers. The sum of maximum variable change at each iteration step is shown. At a high compressibility ($\delta = 4\times10^{-2}$), the solution converges much more slowly as compared with the case of low compressibility ($\delta = 4\times10^{-4}$). The comparison between high compressibility and low compressibility is facilitated by maintaining $Re_{ss} = 818.18$ and $\alpha = 1.1$.

Weakly compressible Newtonian flow

In order to test the numerical model and solution algorithm, the modeled pipeline is assumed to be filled with a weakly compressible Newtonian fluid. A flow calculation is performed for the case described by $\delta = 8\times10^{-2}$ and $Re = 0.0884$, and $L/R = 200$. In order to provide a completely coordinated comparison with literature results, the dimensionless time variable used by Vinay et al.[11] is implemented instead of the scheme presented in Eq. 9. Thereby, a highly accurate matching of the pressure evolution is found (Figure 4a), confirming a correct algorithm as verified by a detailed comparison with the results of Vinay et al. In this example, due to low Reynolds number and high compressibility, the acoustic wave is attenuated by viscous effects.

Figure 6b shows the propagation of the acoustic wave at a moderate value of $Re_{ss} = 2.2$ and $\delta = \chi_\Theta p = 4\times10^{-4}$. For the acoustic wave simulation, the dimensionless time given in Eq. 9 is used. To analyze the compression front propagation, a non-dimensional front propagation velocity of ~0.243 is calculated from Figure 4b. In dimensional form, the compressional front speed can be written as

$$v_f = \frac{z}{t} = \frac{\hat{z}L}{\hat{t}\delta L_s/W_s} = 3.33\times10^2\ \mathrm{m/s}.$$

In this case, the parameter values $\alpha = 1.1$, $W_s = 0.5$ are considered, where the pressure is 4000 Pa and $\chi_\Theta = 10^{-8}$ Pa^{-1}. The analytical acoustic wave propagation velocity is

$$v_f \approx \sqrt{\frac{1}{\chi_\Theta \rho_0}} = 3.33\times10^2\ \mathrm{m/s}.$$

The matching value of the pressure propagation front speed and acoustic speed calculated from the analytical expression further confirms the accuracy of the solution algorithm.

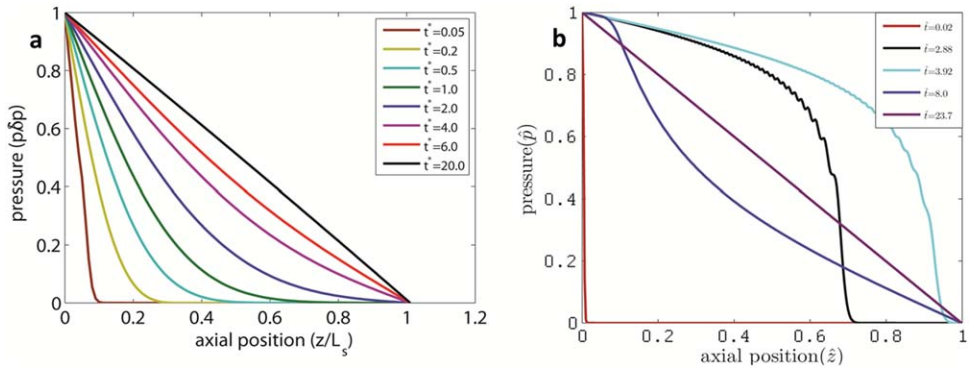

Figure 4. Evolution of the pressure profile at the center of the pipeline for a Newtonian compressible fluid (a) δ=8 $\times10^{-2}$ and $Re_{ss} = 0.0884$ and (b) $\delta = 8\times10^{-4}$ and $Re_{ss} = 2.2$.

[Color figure can be viewed in the online issue, which is available at wileyonlinelibrary.com.]

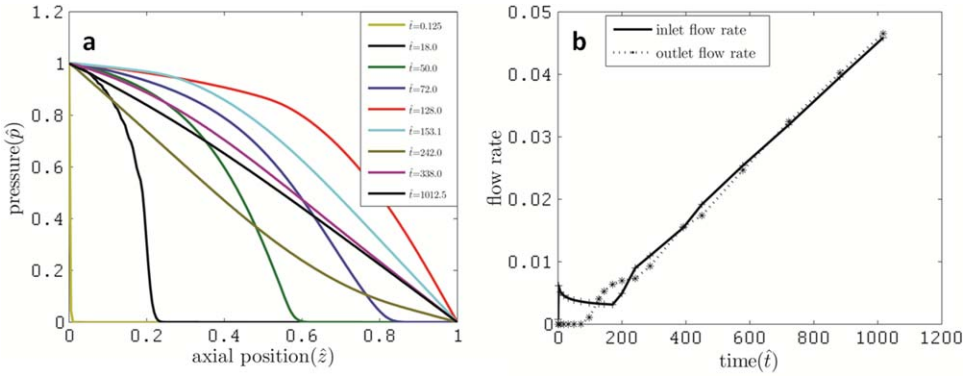

Figure 5. (a) Time evolution of the pressure profiles and (b) time evolution of the inlet and outlet flow rates for a weakly compressible thixotropic flow for $\delta = 4\times10^{-4}$, $\alpha = 1.1$, $\mu_r = 200$ and $Re_{ss} = 818$.

[Color figure can be viewed in the online issue, which is available at wileyonlinelibrary.com.]

Compressible non-Newtonian flow

At time $\hat{t} = 0^+$, pressure propagation commences. In an idealized analysis, the displacing fluid exerts compressional stress upon the first gelled segment via inertial compression. A relatively small deformation accompanies the inertial compression process. The inertial compression is followed by viscous strain accumulation. Accumulated viscous deformation causes gel degradation.

Computations are performed with the parameter values $\delta = 4.0\times10^{-4}$, $\alpha = 1.1$, $\mu_r = 200$, and $Re_{ss} = 818.18$. The pressure profile evolution with time is shown in Figure 5a. Stress localization processes are confined to the axial pipe direction. Axial stress localization and radial shear localization are dissimilar phenomena, but both have a large impact on pipeline restart processes. The applied pressure in Figure 5a represents a flow where inertial effects are present. In this analysis the effective Reynolds number changes with the degree of gel degradation. The final, asymptotic value of the Reynolds number is defined as the steady state Reynolds number and denoted by Re_{ss}. The pressure profile exhibits a high axial gradient at the compression front. The pressure propagation front initially travels at a nearly constant non-dimensional velocity ($\sim10^{-2}$) and the same holds true for physical velocity. Hence, it can be inferred that the nature of the pressure propagation is inertial. After the pressure front reaches the pipe outlet, the pressure profile is reflected backwards as a result of the zero pressure boundary condition at the outlet. This is due to what can be referred to as "inertial puncture." "Inertial puncture" is defined by the fact that when the pressure reaches the outlet, some fluid exits the pipe in the presence of the pressure gradient at the interface, causing excess pressure release and sudden pressure reduction. This is also confirmed in Figure 8, where the outlet flow rate evolution shows positive flow at the time when the pressure signal reaches the exit, $\hat{t}\sim100$. Therefore, the pressure profile is reflected backwards. The "inertial puncture" process for gelled fluids is demonstrated for the first time in the current work. The evolution of the inlet and outlet flow rates is shown in Figure 5b. Initially, the inlet flow rate decreases as the pressure propagates along the pipeline. This reduction is expected due to viscous dissipation behind the compression front. The outlet condition remains quiescent until $\hat{t}\sim100$, due to the finite pressure propagation speed. Gel breakdown results in increased inlet flow, as the viscosity is reduced as a result of gel degradation. Therefore, in order to push an identical volume of fluid, a smaller pressure gradient is required, as the viscous resistance decreases. Hence, the inlet flow increases at time $\hat{t}\sim180$, and after a transmission lag, the outlet flow also increases. The time lag between increases in inlet and outlet flow rates is explained by the fact that pressure propagation is a noninstantaneous process. Eventually, the inlet and outlet mass flow rates converge after a transient process is completed and a quasisteady state is achieved. The true steady state, with constant flow rates, is achieved only after a much longer time, when either gel breakdown is complete or convective flow removes all the gel. In this article, simulations are carried out up to the true steady state only for a few high compressibility cases due to the very long computational time requirements.

Furthermore, our time dependent evolution of the outlet flow rate profile follows a similar trend to the pressure evolution profile at the interface of the gel and downstream fluid as reported by El-Gendy et al.[29] The fluid flow rate in the downstream (Newtonian fluid) varies linearly with the pressure at the gel and water interface providing a direct comparison of our outlet flow rate with the reported pressure profile.[29] Moreover, a qualitative comparison is also possible between our inlet flow rate and the experimental results of Borghi et al.[26] and Margarone et al.[27] Borghi et al. and Margarone et al. work mainly deals with constant flow rate experiments while our study deals with constant inlet pressure condition. However, the nature of pressure evolution at inlet in flow rate controlled restart, and inlet flow rate evolution in pressure controlled study can appropriately be compared. Initially, the inlet flow rate in our study decreases as the applied pressure needs to counter additional viscous dissipation in the downstream of the pipeline. For the same reason in the constant flow rate case, inlet pressure increases in order to maintain a constant flow. Once the gel starts breaking, the inlet pressure decreases due to a decrease in viscous dissipation. In our case, inlet flow rate starts increasing as a result of gel breakage.

To further analyze compression front propagation at the initial time, a non-dimensional front propagation velocity of ~0.0115 is calculated from Figure 5a. With time, the pressure propagation slows down due to viscous effects as can be seen in Figure 5a. The compression front speed at the initial time can be calculated in dimensional form as

$$v_f = \frac{z}{t} = \frac{\hat{z}L}{\hat{t}\delta L_s/W_s} = 3.16\times10^2\ \mathrm{m/s}.$$

As before, the acoustic wave propagation velocity is 3.33×10^2 m/s. The appropriate comparison between theoretical

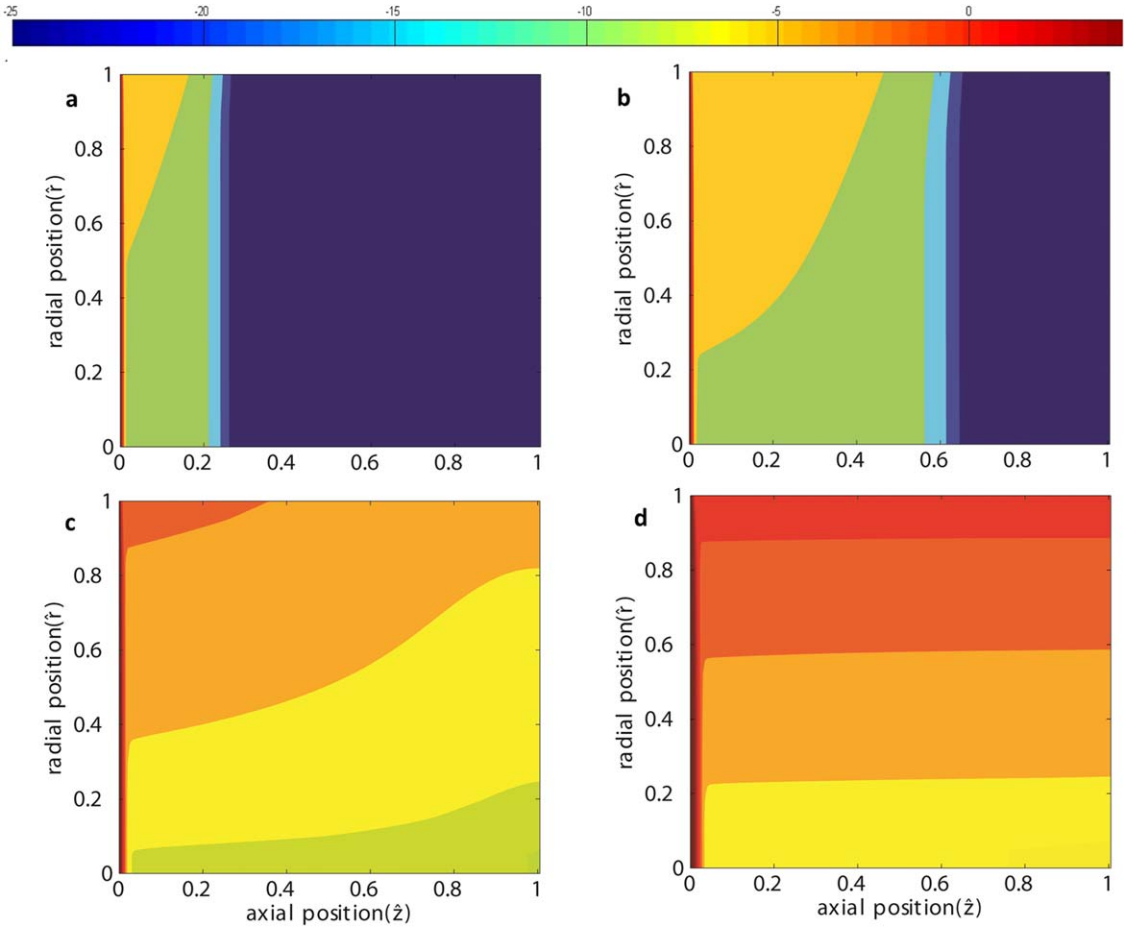

Figure 6. Time evolution of the absolute strain inside the pipeline for a weakly compressible thixotropic flow showing pressure propagation and extent of deformation for $\delta = 4\times10^{-5}$, α=1.1, μ_r= 200, and Re_{ss}= 818 (a) $\hat{t}$= 18.0, (b) $\hat{t} = 50.0$, (c) $\hat{t} = 72.0$, and (d) $\hat{t} = 128.0$.

[Color figure can be viewed in the online issue, which is available at wileyonlinelibrary.com.]

and computed propagation velocity confirms an acoustic wave at low gel strength and high Re_{ss} conditions. However, for high gel strength conditions, where the viscous effect dominates, the compression front velocity is much smaller than the acoustic velocity.

The gel breakdown phenomenon begins as soon as the pressure propagation commences (Figure 6). Contour plots show representative strain distributions. At strain values above 5000, the gel structure is assumed to be completely broken down. The color variation indicates the extent of degradation on a logarithmic scale. Dark blue represents the pristine gel and red represents the degraded gel slurry. Fresh oil is represented by completely degraded slurry (dark red). Note that the colours are based on a log scale with many decades.

At $\hat{t} = 0+$, fresh fluid displaces the gelled crude oil by exertion of a high constant pressure. The initial response of the gel is captured at $\hat{t} = 18$. The pressure commences penetrating the gel simultaneously to the compression. The leading edge of the pressure front is transmitted past a given fluid element even as the compression of the given element continues. Behind the front, strain is increased near the wall, as shown in Figure 6a, with almost constant strain value in the core regions. At the wall, no slip boundary conditions apply. Therefore, the additional strain emanates from the wall. This shear effect does not become significant instantaneously. With time, the pressure propagates further downstream. At $\hat{t} = 50$ (Figure 6b), the leading edge of the pressure has reached $\hat{z} \sim 0.6$ from the entrance. The shear strain accumulates near the wall, and the total strain becomes the dominant rheological influence near the wall. This process is clearly evident in Figure 6c (at $\hat{t} = 72$). Figure 6d shows strain contours in the pipeline at $\hat{t} = 128$, when the axial variation has diminished. Note that the orange-red colour in Figure 6d indicates a strain of about 10^{-2}, many orders of magnitude less than that required for complete gel breakdown. The gel has undergone sufficient time for shear accumulation. From Figure 5b it is also evident that after the pressure signal has reached the outlet, strain accumulates and inlet flow rate increases. Shear strain accumulation causes additional gel breakdown and concomitant viscosity reduction. Evolution of the outlet velocity profile is shown in Figure 7, further confirming breakage-induced flow acceleration.

Effect of gel strength

Various viscosities are considered in order to analyze the effect of gel strength on the pressure propagation process. An initial viscosity of 10^4 Pa·s is selected to emulate a high gel strength, and an initial viscosity of 10^2 Pa·s is used to emulate a weak gel. At high viscosity, inertial effects become insignificant and the pressure evolution process is dominated by viscous effects and gel degradation, as shown

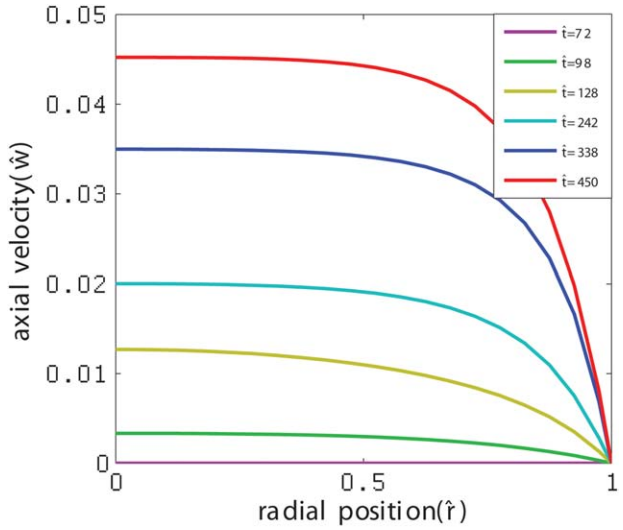

Figure 7. Time evolution of the outlet velocity profiles for a weakly compressible thixotropic flow with $\delta = 4\times10^{-4}$, $\alpha = 1.1$, $\mu_r = 200$, and $Re_{ss} = 818$.

[Color figure can be viewed in the online issue, which is available at wileyonlinelibrary.com.]

in Figure 8a. The pressure profile decay appears to be an exponential function of axial position, similar to the Newtonian flow case at low *Re* (Figure 4a). At the initial time a small increase in pressure appears which looks like an artifact of the numerical algorithm. However, a similar effect has been reported by Cawkwell et al.[5] and Vinay et al.[11] for weakly compressible flow simulation. Cawkwell et al. attributed the initial rise in pressure to weak compressibility and inertial effects. Furthermore, Ei-Gendy et al.[29] also experimentally found a similar rise in pressure at the initial time. Moreover, the initial rise in pressure can be explained by the fact that a Newtonian fluid (displacing fluid) with inertia pushes a stationary gel. The inertia can be transferred to increase the pressure. Furthermore, the pressure profile in Figure 8a is consistent with the non-linear pressure profile observed by Ei-Gendy et al.[29] and inlet flow rate (Figure 8b) is consistent with inlet pressure profile reported by Borghi et al.[26] and Margarone et al.[27]

If the initial viscosity is two orders of magnitude higher than the weak gel case, the effective initial Reynolds number becomes four orders of magnitude lower due to the variable group inherent in the Reynolds number definition. The effective Reynolds number increases with time as the gel breaks. Hence, pressure propagation prior to breakage is dominated by viscous effects. The final stage is characterized by complete breakage. In the final stage, the flow properties for both high and low initial gel strength cases are identical due to the coordinated final gel condition. As evident from Figure 8a, when the pressure signal reaches the pipe outlet, upstream viscous strain accumulation causes gel breakdown and concomitant viscosity reduction. Thus, the pressure profile flattens near the entrance, facilitating axial stress localization in downstream pipe segments, effectively promoting restart. Figure 8b shows the inlet-outlet flow rate evolution with time. The effect of viscosity on the flow profile is illustrated. From Figure 5b, it is evident that fluid exits the pipe at $\hat{t}\sim100$ for the weak gel. However, in the case of a strong gel, with all other conditions the same, the exit flow starts at $\hat{t}\sim4500$ (Figure 8b). Therefore, it can be concluded that the stronger gel requires a much longer period of pressure application to restart, in this case 45 times more.

Effect of compressibility

The effect of compressibility on pressure propagation is analyzed by considering the compressibility numbers $\delta = 4\times10^{-2}$ and $\delta = 4\times10^{-6}$. The remaining parameters are fixed as $\alpha = 1.1$, $\mu_r = 200$, and $Re_{ss} = 818.18$. The nature of pressure propagation is similar to the case of $\delta = 4.0\times10^{-4}$, while the axial pressure gradient at the compression front sharpens as shown in Figures 9a and b. From Figure 9 it is clear that at both at high and low compressibility, small wave-like oscillations are superimposed on the pressure profile, due to numerical discretization. As the pressure propagates further into the gel, the oscillations are damped out and the pressure profile becomes smooth. At the initial unbroken state (where viscosity is 200 times higher than steady state), the magnitude of the effective Reynolds number becomes similar to that of the compressibility number $\delta = 4\times10^{-2}$, causing an initial wave-like oscillation. When the compressibility number and Reynolds number have similar values, there is a balance between the time scales for pressure diffusion and velocity transit relaxation, enabling oscillations to propagate in the pipeline, as discussed by Vinay et al.[12] For $\delta = 4\times10^{-6}$, the compression front is transmitted quickly and viscous damping does not have time

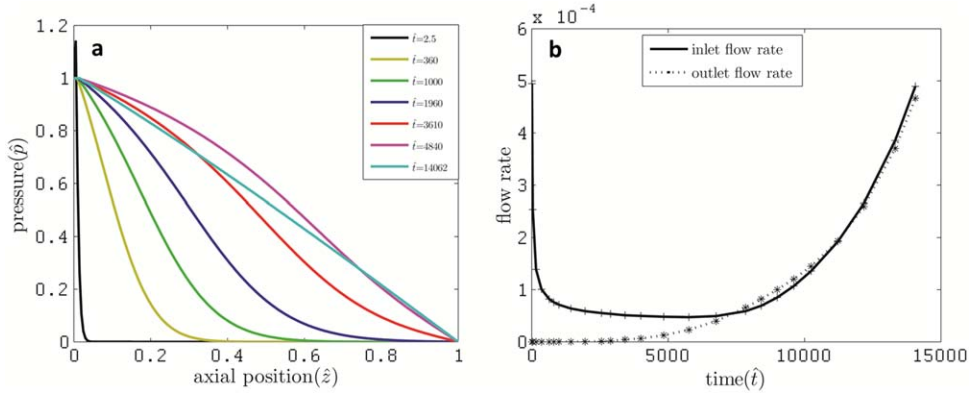

Figure 8. Time evolution of (a) pressure profiles (b) inlet and outlet flow rates for a weakly compressible thixotropic flow with $\delta = 4\times10^{-4}$, $\alpha = 1.1$, $\mu_r = 2\times10^4$, and $Re_{ss} = 818$.

[Color figure can be viewed in the online issue, which is available at wileyonlinelibrary.com.]

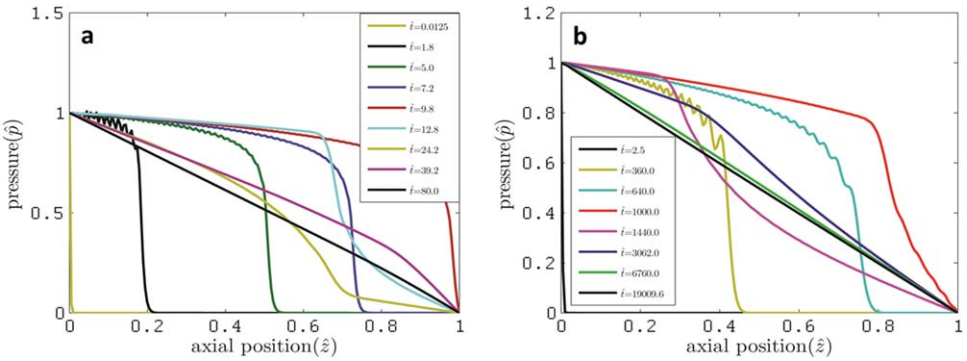

Figure 9. Time evolution of pressure profile for a weakly compressible thixotropic flow for (a) $\delta = 4\times10^{-2}$ and (b) $\delta = 4\times10^{-6}$, while $\alpha = 1.1$, $\mu_r = 200$ and $Re_{ss} = 818$.

[Color figure can be viewed in the online issue, which is available at wileyonlinelibrary.com.]

to dissipate the oscillations, thus wave-like oscillations are observed for a longer period. Furthermore, it is evident from Figure 9 that both increasing and decreasing compressibility make the compression front sharper. In the case of high compressibility, downstream pressure propagation results in high deformation and rapid gel breakdown. Therefore, viscous dissipation in the broken gel is lower and the energy consumed by compression is dominant at the compression front.

However, at low compressibility, pressure propagation proceeds quickly and viscosity is unable to flatten the compressional front before the pressure propagation front proceeds downstream, similar to inviscid flow. Viscous damping strongly depends on gel strength. If the gel strength is high, wave-like oscillations are not observed due to fast viscous attenuation. Figures 10a and b show inlet and outlet flow rates in the cases of $\delta = 4\times10^{-2}$ and $\delta = 4\times10^{-6}$, respectively. From Figure 10a, it can be concluded that, after a transition period, the flow approaches a true steady value. In the other cases, the flow is also expected to reach a true steady state. However, it is computationally expensive to achieve. Hence, for other cases the solution is not computed all the way to the true steady state values.

From Figure 11, it may be inferred that for highly compressible gels, strain accumulates faster as a result of additional deformation near the wall. From Figures 11a and b, it may be confirmed that significantly more near-wall breakdown occurs as the pressure propagates through a local segment. When the pressure signal passes a local gel segment, significant strain occurs nearly instantaneously. Due to the rapid gel breakdown process, the pressure front remains relatively sharp. Fresh fluid has not penetrated a long distance from the entrance by convection before the near-wall gel breaks down at the pipe inlet. The dark red color corresponds to fresh fluid. The convective flow effect is observed close to the entrance; the gel breakdown phenomenon is dominant due to viscosity reduction. The governing phenomena in the restart process are gel breakdown and compressibility. Furthermore, it is illustrated in Figures 11c and d that large scale convective flow follows near-wall gel breakdown. Furthermore, it shows significant displacement of the gel initially present in pipeline by fresh fluid.

To examine various values of the compressibility number, $\delta = 4\times10^{-3}$ and $\delta = 4\times10^{-5}$are considered while the other parameters are fixed. The pressure profiles corresponding to these parameters are shown in Figure 12a and b. It is clear from these figures that the small oscillations can be reduced either by increasing the compressibility from a lower (Figure 9a) to a higher value (Figure 12a) or by decreasing the compressibility from a higher (Figure 12b) to a lower value (Figure 12b). The mechanisms for small oscillatory wave propagation were discussed. The changes in compressibility number result in deviations from these mechanisms.

In Figures 13a and b, pressure profile evolution is shown for $\delta = 4\times10^{-2}$ and $\delta = 4\times10^{-6}$, respectively for $\mu_r = 2\times10^4$, while other parameters are fixed. At high viscosity, the pressure exhibits a near exponential decay profile in space for $\delta = 4\times10^{-6}$, which qualitatively matches with the

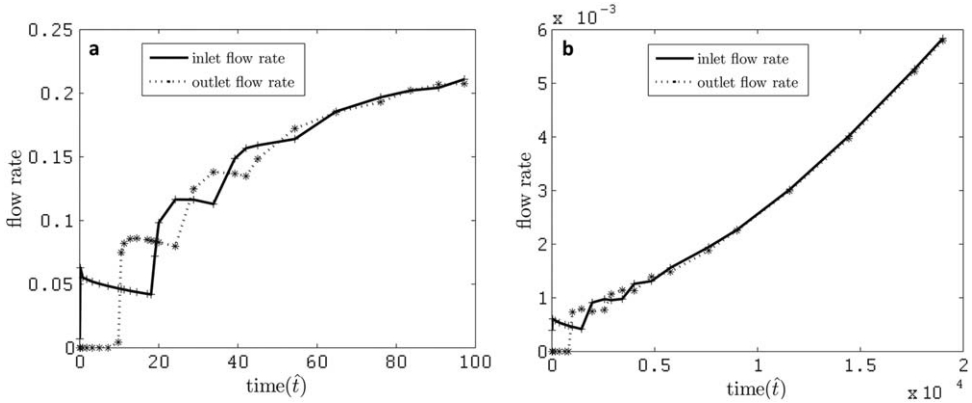

Figure 10. Time evolution of the inlet and outlet flow rates for a weakly compressible thixotropic flow for (a) $\delta = 4\times10^{-2}$ and (b) $\delta = 4\times10^{-6}$, while $\alpha = 1.1$, $\mu_r = 200$ and $Re_{ss} = 818$.

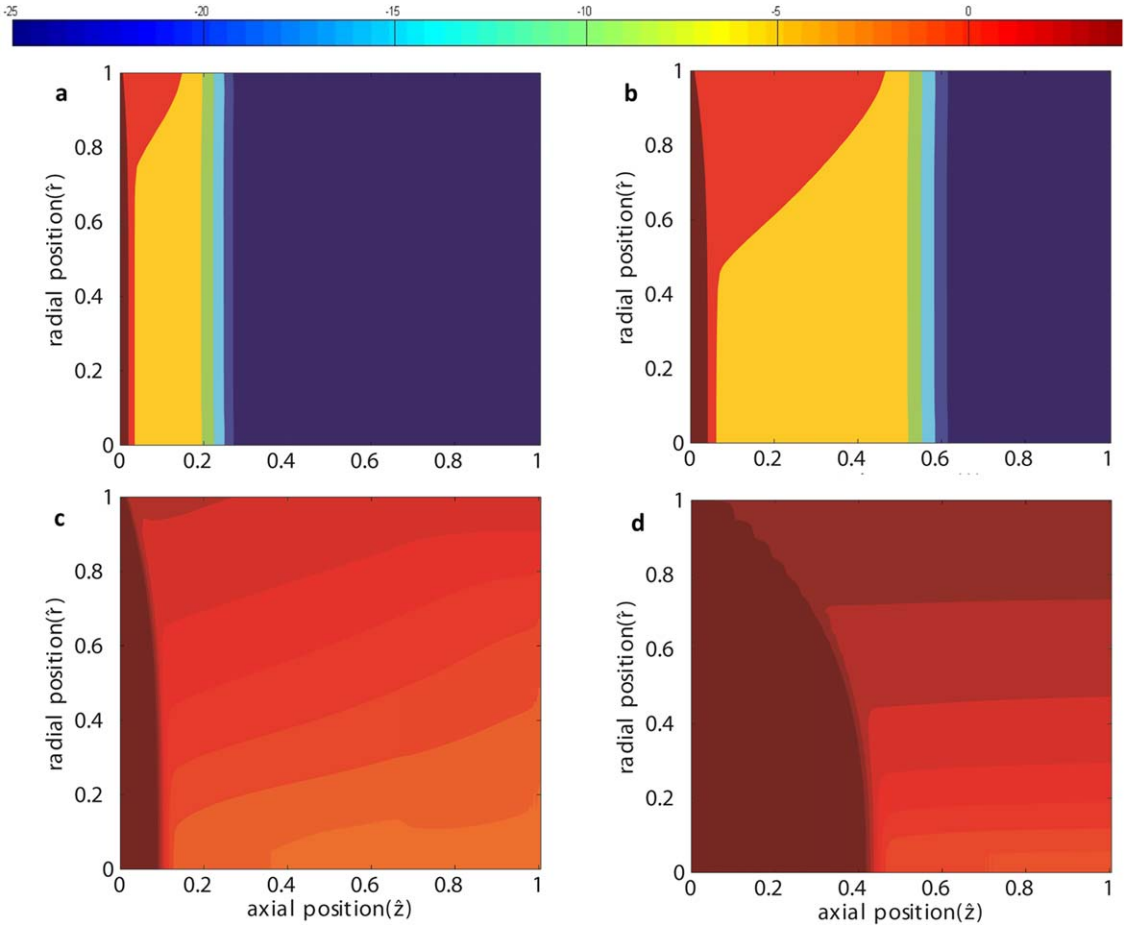

Figure 11. Time evolution of the absolute strain inside the pipeline for a weakly compressible thixotropic flow showing pressure propagation, extent of deformation, and penetration of fresh fluid for $\delta = 4\times10^{-2}$, $\alpha = 1.1$, μ_r=200, and $Re_{ss} = 818$ (a) $\hat{t} = 18.0$, (b) $\hat{t}$= 128.0, (c) $\hat{t}$= 288.0, and (d) $\hat{t}$= 800.0.

[Color figure can be viewed in the online issue, which is available at wileyonlinelibrary.com.]

results of El-Gendy et al.[29] High viscosity severely dampens the pressure propagation. Moreover, low compressibility results in significantly less deformation in the gel, which is not sufficient to cause breakdown. Hence, the pressure profile is found to follow an exponential decay with respect to axial position, similar to the viscosity-dominated flow regime. A two order of magnitude increase in viscosity causes a four order of magnitude reduction in the effective Reynolds number at the initiation of the restart process. However, at high compressibility ($\delta = 4\times10^{-2}$), gel breakdown is much faster and the viscosity is reduced as soon as the pressure signal passes a local gel segment. Hence, the pressure propagation is dominated by gel degradation. This phenomenon leads to a sharp gradient at the compression front even for strong gels. In Figure 14, the evolution of the inlet and outlet flow rates with time is shown, corresponding

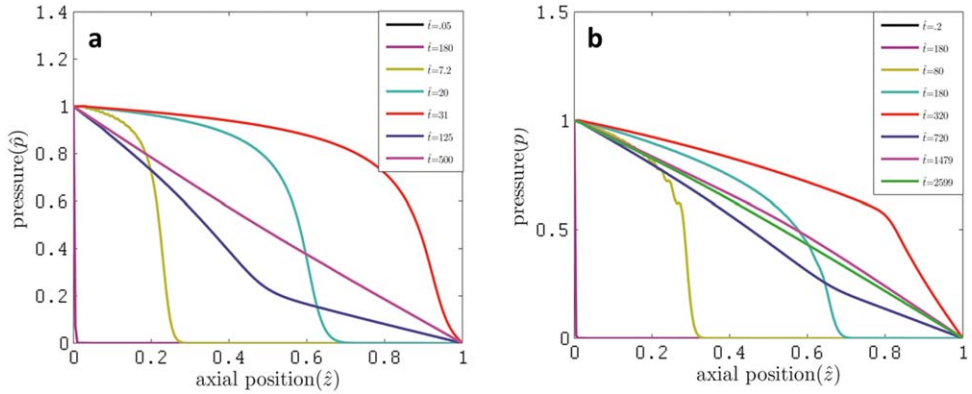

Figure 12. Time evolution of the pressure profile for a weakly compressible thixotropic flow for (a) $\delta = 4\times10^{-3}$ and (b) $\delta = 4\times10^{-5}$, $\alpha = 1.1$, μ_r= 200, and $Re_{ss} = 818$.

[Color figure can be viewed in the online issue, which is available at wileyonlinelibrary.com.]

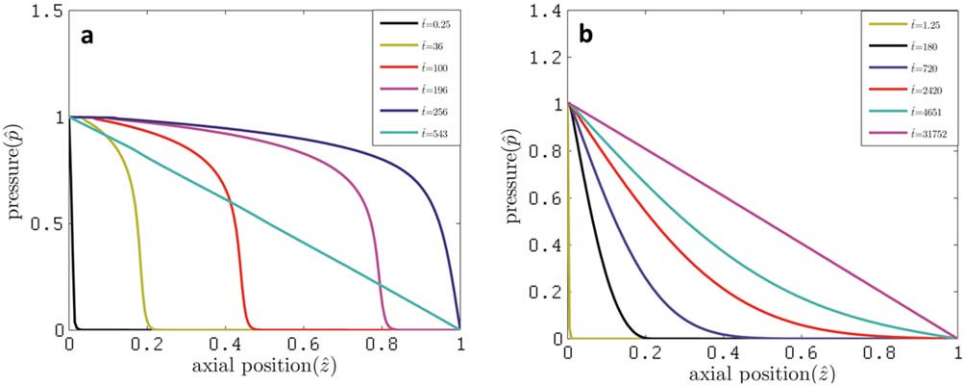

Figure 13. Time evolution of the pressure profile for a weakly compressible thixotropic flow for (a) $\delta = 4\times10^{-2}$ and (b) $\delta = 4\times10^{-6}$, $\alpha = 1.1$, $\mu_r = 2\times10^4$, and $Re_{ss} = 818$.

[Color figure can be viewed in the online issue, which is available at wileyonlinelibrary.com.]

to the pressure profiles in Figure 13. For high gel strength and high compressibility (Figure 14a), the outlet flow becomes positive at $\hat{t}\sim250$ which is 25 times higher than low gel strength condition (Figure 10a). This is consistent with earlier observations. From these Figures, it can also be inferred that to reach a true steady state condition (to displace all the gel present in the pipeline), the time required is only 6 times more for the strong gel compared to the time required for the initial pressure signal propagation which is 25 times greater. Figures 10a and 14a show that for both strong and weak gel conditions, the final flow becomes identical. Furthermore, Figure 14b along with Figures 8b and 5b explain the delayed breakage in the gel. The weak gel (Figure 5b) breaks quickly compared to the strong gel (Figure 8b) at same applied pressure which is obvious. However, for the same gel strength as Figure 8b, in the low compressible gel case, the pressure propagates much faster (Figure 14b) and maintains constant pressure gradient. In this case, gel breakage is a very slow process (Figure 14b). Hence, the simulation has not been performed until the gel breakage becomes significant because of computational time constraints. Here, the flow rate increment refers to gel breakage. A similar trend of gel breakage has been reported in the rheometer length scale by Magda et al.[33]

Effect of pipeline dimension and Re_{ss}

To illustrate the effect of the Reynolds number on the pressure propagation, Re_{ss} is varied by altering either the input pressure or α. Pressure alteration effectively changes the value of L_s (i.e., pipeline length, $L = \alpha L_s = \alpha R/\varepsilon$). Therefore, in order to maintain the pipe dimension at dissimilar applied pressures, α and ε are adjusted. For a long pipe, with $\varepsilon = 1/100$, $\alpha = 17.6$ (length to radius ratio 1760), $\mu_r = 200$, $\delta = 4\times10^{-4}$and $Re_{ss} = 51$, Figure 15 shows different pressure evolution profiles. In order to maintain Re_{ss}, smaller applied pressure and pipeline length are used. Extraneous parameters are $\varepsilon = 16/100$, $\alpha=17.6$ (length to radius ratio 110), $\mu_r = 200$, and $\delta = 4\times10^{-4}$. Although Re_{ss} is identical in both cases, in the first case a larger initial pressure is exerted upon the entrance gel. The effect is comparable to the inertial regime discussed earlier with a high Re_{ss}. In the second case, a lower initial pressure is exerted on the entrance gel and the nature of pressure propagation is similar to viscous dominated compression flow.

The inlet and outlet flow rates are shown in Figures 16a and b, corresponding to the pressure profiles shown in Figures 15a and b, respectively. Even at identical Re_{ss} the plots of inlet and outlet flow rates are very different. In Figure 16a, both the inlet and outlet flow rates oscillate prior to converging. However, Figure 16b does not indicate oscillation, and converges similar to low Reynolds number Newtonian flow. This is unexpected, as the same Reynolds number would be expected to give similar flow properties. However, for longer pipelines, the applied pressure is higher which may lead to additional gel breakdown compared to shorter pipes with low pressure, irrespective of an identical value of

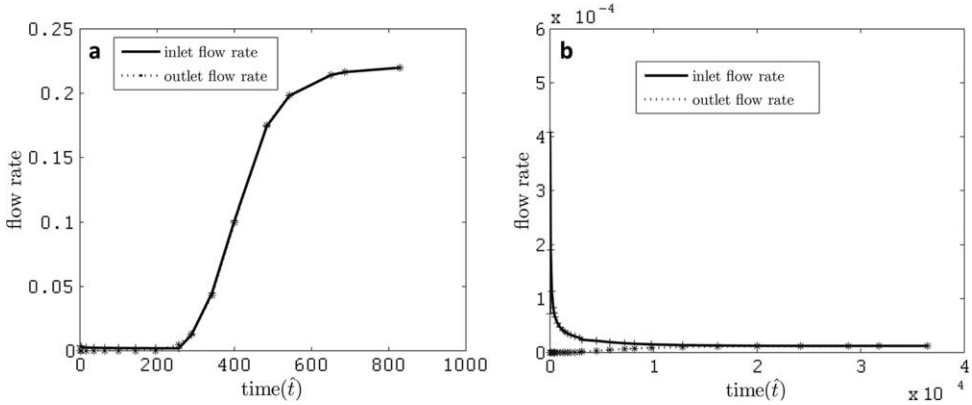

Figure 14. Time evolution of the inlet and outlet flow rates for a weakly compressible thixotropic flow for (a) $\delta = 4\times10^{-2}$ and (b) $\delta = 4\times10^{-6}$, $\alpha = 1.1$, $\mu_r = 2\times10^4$, and $Re_{ss} = 818$.

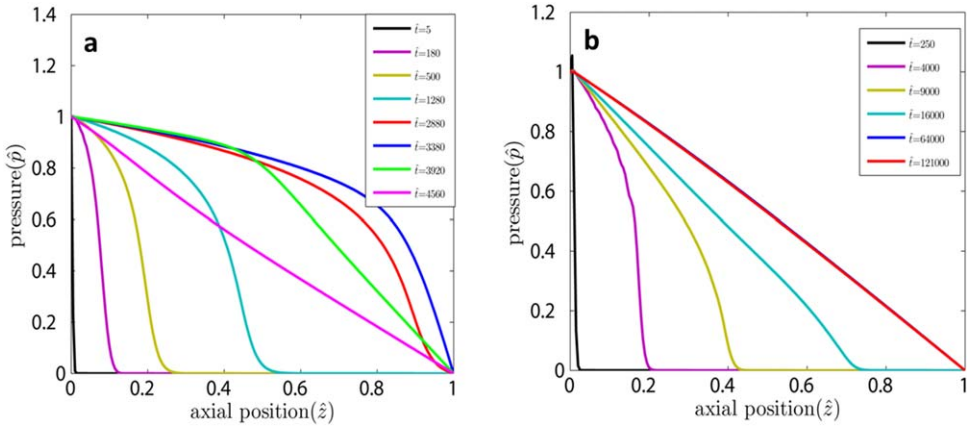

Figure 15. Time evolution of the pressure profile for a weakly compressible thixotropic flow for (a) $\varepsilon = 1/100$ and (b) $\varepsilon = 16/100$ other parameters are $\delta = 4\times10^{-4}$, $\alpha = 17.6$, viscosity ratio of gel and broken crude oil 200 and $Re_{ss} = 51.13$.

[Color figure can be viewed in the online issue, which is available at wileyonlinelibrary.com.]

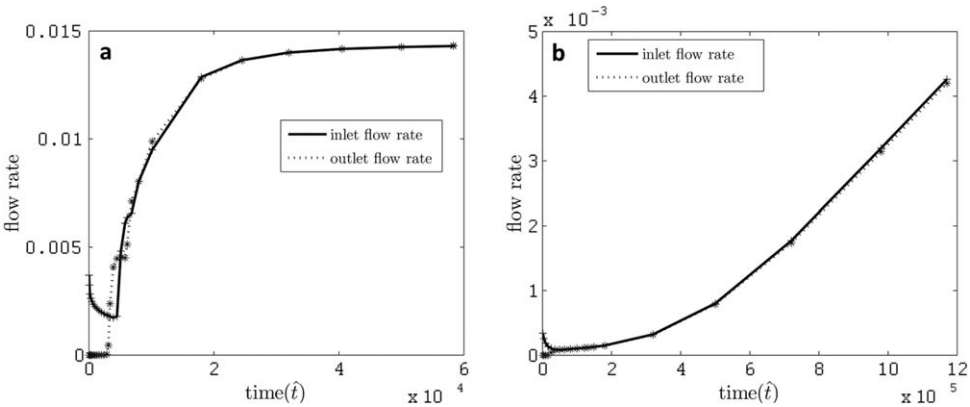

Figure 16. Time evolution of the inlet and outlet flow rates for a weakly compressible thixotropic flow for (a) ε= 1/100 and (b) $\varepsilon = 16/100$ other parameters are $\delta = 4\times10^{-4}$, $\alpha = 17.6$, $\mu_r = 200$ and $Re_{ss} = 51.13$.

Re_{ss}. Furthermore, delayed pressure propagation in the longer pipe provides additional time for shear accumulation and gel breakdown. These phenomena contribute to the difference in pressure propagation even at identical Reynolds number. Finally, it is worth mentioning that pressure profile for high aspect ratio qualitatively matches with the pressure profile reported by Borghi et al.[26]

To illustrate the effect of Re_{ss} as well as compressibility, the evolution of the inlet and outlet flow rates is presented for various sets of parameters in Figures 17a and b. In this case, the time scale is converted to match the case of $\delta = 4\times10^{-4}$ and $Re_{ss} = 818.18$ for appropriate comparison. The parameter α is adjusted to match the actual pipeline length. It is evident from Figure 17b that the gel emerges from the pipe faster in the case of low compressibility, due to faster propagation of the pressure signal. For $\delta = 4\times10^{-5}$ and $Re_{ss} = 818.18$, the gel emerges from the pipe outlet at $\hat{t} = 100$. For $\delta = 4\times10^{-4}$ and $Re_{ss} = 818.18$, the gel emerges

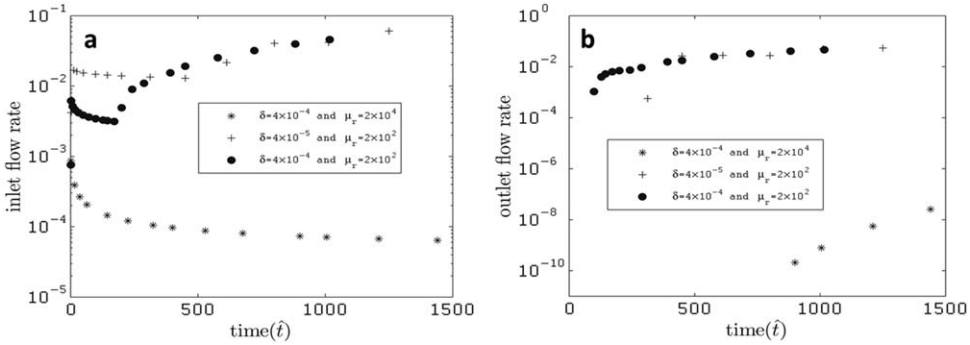

Figure 17. Time evolution of (a) inlet flow rates, and (b) outlet flow rates, for a weakly compressible thixotropic flow for different systems with a single time scale corresponding to the parameters $\delta = 4\times10^{-4}$, $\alpha = 1.1$, and $Re_{ss} = 818$.

from the pipe outlet at $\hat{t} = 300$. Hence, a tenfold decrease in compressibility increases the pressure propagation time by a factor of three. After outlet flow commencement, the compressibility has no impact on the outlet and inlet flows, as shown in Figures 17a and b. Therefore, it is concluded that compressibility plays a dominant role only during the initial pressure wave propagation, and not during the subsequent creep or transient flow acceleration phases. However the initial pressure propagation process governs pipeline restart in most cases, as it determines whether or not flow will commence within a reasonable time.

Conclusion

A 3-D axisymmetric model has been developed to predict weakly compressible transient flow of irreversible thixotropic fluids. Combined effects of inertia, viscosity and gel breakdown govern the pressure wave propagation process. The rheology model comprises a strain-dependent apparent viscosity. To facilitate a stable solution, a finite volume method on staggered grid is implemented with an iterative predictor-correction solution algorithm.

Compressibility, gel strength and thixotropy play pivotal roles in the pressure wave propagation and pipeline restart process for homogenous gels. Elevated compressibility assists in breaking the waxy crude gel structure due to higher local deformation. Thixotropy plays a larger role in systems with larger pipe diameters and larger pipe lengths, giving a tendency toward-radial shear localization and axial stress localization, respectively. Gel thixotropy compensates for a lower applied pressure by reducing the effective viscosity, although a longer restart time is required. Finally, it is shown that the shear localizes near the wall. The gel breaks near the wall prior to convective flow penetration. The model may be readily extended to multipocket gels.

Pressure propagation is dominated by three separate regimes: inertial, viscous, gel degradation. Their combined effects are also clearly illustrated in this article. At low initial viscosity (weak gel), the pressure propagation is dominated by inertial flows. At high initial viscosity (strong gel), pressure propagation is dominated by viscous effects after the initial inertial wave is quickly attenuated by viscosity. At high compressibility and high viscosity, pressure propagation is dominated by gel degradation, as rapid gel degradation causes viscosity reduction and maintains a sharp pressure front. Due to combined effects of these phenomena, it has been shown that pressure propagates with near acoustic speed in a weak gel. The increase in gel strength causes several order of decrease in the pressure propagation speed. Furthermore, decrease in compressibility causes increase in pressure propagation speed. Longer pipes show phenomenon sharp pressure front, even for moderate compressibility due to additional strain accumulation and gel breakage.

For thixotropic weakly compressible fluid, critical pressure depends on compressibility and gel degradation kinetics in addition to gel strength. On one hand, for very weakly compressible fluid, pressure propagates without gel degradation. Hence flow may not restart even after successful pressure propagation. And on the other hand, for highly compressible fluid, gel degradation is sequential in nature which makes sure that the flow commences for long pipeline. For intermediate compressibility depending on the gel strength, flow may restart in the pipeline which is longer than critical length. It is to be noted that in the case of purely viscous rheology without structure build-up, pressure always propagates in the pipeline. So here flow restart is referred by, flow restart within experimental time scale and if flow does not restart in experimental time scale of restart it is referred as no flow restart case.

Acknowledgments

The authors acknowledge Petronas, Petrobras, Statoil ASA, Champion Technologies, BASF, and the Research Council of Norway for their financial support and Olaf Skjæraasen from the Institute for Energy Technology, Kjeller for critically reading this manuscript. Lalit Kumar also thanks Dr. Enrico Riccardi for introducing him to the Linux system.

Literature Cited

1. da Silva JAL, Coutinho JA. Dynamic rheological analysis of the gelation behaviour of waxy crude oils. *Rheol Acta*. 2004;43(5):433–441.
2. Lee HS, Singh P, Thomason WH, Fogler HS. Waxy oil gel breaking mechanisms: adhesive versus cohesive failure. *Energy Fuels*. 2007;22(1):480–487.
3. Pedersen KS, Rønningsen HP. Influence of wax inhibitors on wax appearance temperature, pour point, and viscosity of waxy crude oils. *Energy Fuels*. 2003;17(2):321–328.
4. Visintin RF, Lapasin R, Vignati E, D'Antona P, Lockhart TP. Rheological behavior and structural interpretation of waxy crude oil gels. *Langmuir*. 2005;21(14):6240–6249.
5. Cawkwell M, Charles M. An improved model for start-up of pipelines containing gelled crude oil. *J Pipelines*. 1987;7:41–52.
6. Cawkwell M, Charles M. Characterization of Canadian arctic thixotropic gelled crude oils utilizing an eight-parameter model. *J Pipelines*. 1989;7:251–264.
7. Chang C, Nguyen QD, Rønningsen HP. Isothermal start-up of pipeline transporting waxy crude oil. *J Non-Newtonian Fluid Mech*. 1999;87(2):127–154.
8. Davidson MR, Dzuy Nguyen Q, Chang C, Rønningsen HP. A model for restart of a pipeline with compressible gelled waxy crude oil. *J Non-Newtonian Fluid Mech*. 2004;123(2):269–280.
9. Davidson MR, Nguyen QD, Rønningsen HP. Restart model for a multi-plug gelled waxy oil pipeline. *J Pet Sci Eng*. 2007;59(1):1–16.
10. Sestak J, Charles M, Cawkwell M, Houska M. Start-up of gelled crude oil pipelines. *J Pipelines*. 1987;6(1):15–24.
11. Vinay G, Wachs A, Agassant J-F. Numerical simulation of weakly compressible Bingham flows: the restart of pipeline flows of waxy crude oils. *J Non-Newtonian Fluid Mech*. 2006;136(2):93–105.
12. Vinay G, Wachs A, Frigaard I. Start-up transients and efficient computation of isothermal waxy crude oil flows. *J Non-Newtonian Fluid Mech*. 2007;143(2):141–156.
13. Wachs A, Vinay G, Frigaard I. A 1.5 D numerical model for the start up of weakly compressible flow of a viscoplastic and thixotropic fluid in pipelines. *J Non-Newtonian Fluid Mech*. 2009;159(1):81–94.
14. Houska M. *Inzenyrske Aspekty Reologie Tixotropnich Kapalin*, PhD thesis, Techn. Univ. Prague, Prague, Praha, Czech Republic, 1980.
15. Barnes H, Walters K. The yield stress myth? *Rheol Acta*. 1985;24(4):323–326.
16. Barnes HA. The yield stress—a review or '$\pi\alpha\nu\tau\alpha\ \rho\epsilon\iota$'—everything flows? *J Non-Newtonian Fluid Mech*. 1999;81(1):133–178.
17. Petter Rønningsen H. Rheological behaviour of gelled, waxy North Sea crude oils. *J Pet Sci Eng*. 1992;7(3):177–213.
18. Reiner M. *Lectures on Theoretical Rheology*. Amsterdam, Netherlands: North-Holland Publishing Company, 1960.
19. Liu AJ, Nagel SR. Nonlinear dynamics: jamming is not just cool any more. *Nature*. 1998;396(6706):21–22.
20. Møller PC, Mewis J, Bonn D. Yield stress and thixotropy: on the difficulty of measuring yield stresses in practice. *Soft Matter*. 2006;2(4):274–283.
21. Paso K, Kompalla T, Oschmann HJ, Sjöblom J. Rheological degradation of model wax-oil gels. *J Dispersion Sci Technol*. 2009;30(4):472–480.
22. Teng H, Zhang J. Modeling the thixotropic behavior of waxy crude. *Ind Eng Chem Res*. 2013;52(23):8079–8089.

23. Zhao Y, Kumar L, Paso K, Ali H, Safieva J, Sjöblom J. Gelation and breakage behavior of model wax–oil systems: rheological properties and model development. *Ind Eng Chem Res*. 2012;51(23):8123–8133.
24. Petter RH. Rheological behaviour of gelled, waxy North Sea crude oils. *J Pet Sci Eng*. 1992;7(3):177–213.
25. Perkins T, Turner J. Starting behavior of gathering lines and pipelines filled with gelled Prudhoe Bay oil. *J Pet Technol*. 1971;23(3):301–308.
26. Borghi GP, Correra S, Merlini M, Carniani C. Prediction and scaleup of waxy oil restart behavior. In: *International Symposium on Oilfield Chemistry*. Houston, Texas, USA: Society of Petroleum Engineers, 2003.
27. Margarone M, Gian-Paolo B, Sebastiano C. One dimensional modelling and experimental validation of gelled waxy oil restart. In: *North Africa Technical Conference and Exhibition*. Cairo, Egypt: Society of Petroleum Engineers, 2010.
28. Magda JJ, Elmadhoun A, Wall P, Jemmett M, Deo MD, Greenhill KL, Venkatesan R. Evolution of the pressure profile during the gelation and restart of a model waxy crude oil. *Energy Fuels*. 2013; 27(4):1909–1913.
29. El-Gendy H, Alcoutlabi M, Jemmett M, Deo M, Magda J, Venkatesan R, Montesi A. The propagation of pressure in a gelled waxy oil pipeline as studied by particle imaging velocimetry. *AIChE J*. 2012;58(1):302–311.
30. Billington E. Some measurements of the time dependence of the viscosity of thixotropic fluids. *Proc Phys Soc*. 1960;75(1):40.
31. Kumar L, Lawrence C, Sjöblom J. Mechanism of pressure propagation and weakly compressible homogeneous and heterogeneous thixotropic gel breakage to study flow restart. *RSC Adv* 4.52 (2014): 27493–27501.
32. Wardhaugh LT, Boger DV. The measurement and description of the yielding behavior of waxy crude oil. *J Rheol*. 1991;35(6):1121–1156.
33. Magda JJ, El-Gendy H, Oh K, Deo MD, Montesi A, Venkatesan R. Time-dependent rheology of a model waxy crude oil with relevance to gelled pipeline restart. *Energy Fuels*. 2008;23(3):1311–1315.

Manuscript received Nov. 20, 2013, and revision received Feb. 18, 2015.